Tilt Engineering of Spontaneous Polarisation and Magnetisation Above Room Temperature in a Bulk Layered Perovskite

Michael J. Pitcher[1], Pranab Mandal[1], Matthew S. Dyer[1], Jonathan Alaria[2], Pavel Borisov[1,†], Hongjun Niu[1], John B. Claridge[1*] and Matthew J. Rosseinsky[1*]

[1]Department of Chemistry, University of Liverpool, Crown Street, Liverpool L69 7ZD, United Kingdom.

[2]Department of Physics, University of Liverpool, Liverpool, L69 7ZE, UK

*Correspondence to: m.j.rosseinsky@liv.ac.uk, j.b.claridge@liv.ac.uk

†Current address: Department of Physics, West Virginia University, PO Box 6315, Morgantown, WV 26506, USA.

Crystalline materials that combine electrical polarization and magnetization could be advantageous in applications such as information storage, but these properties are usually considered to have incompatible chemical bonding and electronic requirements. Recent theoretical work on perovskite materials suggested a route for combining both properties in these materials. We used crystal chemistry to engineer specific atomic displacements in a perovskite, $(Ca_xSr_{1-x})_{1.15}Tb_{1.85}Fe_2O_7$ that change its symmetry and simultaneously generate electrical polarization and magnetization. The two resulting properties are magnetoelectrically coupled as they arise from the same displacements.

For many technical applications, crystalline solids must combine distinct properties. For example, in thermoelectrics, thermal and electronic conductivity need to be optimized simultaneously (*1*). This level of structure-property composition control is particularly difficult when the properties have antagonistic chemical requirements. For example, the synthesis of a single phase combining electrical polarization **P** and spontaneous magnetization **M** is hard because of the distinct electronic structure requirements for the main mechanisms producing each property (*2*) *e.g.*, the closed-shell d^0 Ti^{4+} and s^2 Pb^{2+} cations, which produce polarization in the ferroelectric perovskite oxide $PbZr_{1-x}Ti_xO_3$, do not have the unpaired electrons needed for magnetization (*3*). Efficiently combining these two long-range orders could be useful for multiferroic or magnetoelectric information storage, which could overcome the drawbacks of ferroelectric memory (slow writing) and magnetic random access memory (high power density) and opens the possibility of four-state memory (*4, 5*) with reduced energy consumption. It is possible to combine these ground states by making composites over a range of length scales between phases which individually have the chemistry and thus properties required (*6, 7*), or by lowering spatial symmetry through the onset of magnetic order at low temperatures (*8*). We use chemical control of the crystal structure of a single phase material to generate atomic displacements that produce both properties simultaneously in a coupled manner above room temperature.

The chemical incompatibility between **P** and **M** arises when the ferroelectricity is driven by a classical gamma point instability (*9*). Recent theoretical work (*10, 11*) has identified that specific zone-boundary octahedral tilts in an ABO_3 perovskite block coupled to translational symmetry breaking [from A site order in 1:1 perovskite heterostructures or the shearing of adjacent even-numbered $(ABO_3)_n$ blocks by the interposed AO rock salt layer of the $(AO)(ABO_3)_n$ Ruddlesden-Popper (RP) structure (*12*)] can generate hybrid improper ferroelectricity (HIF) without requiring classical zone-center displacements. The polarization in an HIF arises from noncancellation of the antiferrodistortive displacements associated with the tilt at the interfaces between structural blocks. This structure produces an improper ferroelectric, as the primary order parameter is the zone boundary octahedral tilting. HIF is rare because the required structural features are difficult to attain *e.g.*, via artificial cation order in thin-film heterostructures (*13*) or in appropriately tilted bulk n = 2 RP phases, of which there are only three known examples: the nonmagnetic phases $Ca_3Ti_2O_7$*(14)*, which has switchable polarization (*15*), and $Ca_3Ru_2O_7$ (*16*) and the low-temperature magnetically ordered phase $Ca_3Mn_2O_7$ (*17*).

The objective of this study is to combine both polarization and magnetization at room temperature (RT) in a bulk n = 2 RP oxide through control of composition to generate the required octahedral tilts in a system with a strongly magnetic B-site sublattice. For a magnetically ordered oxide insulator operating via superexchange, this requirement can be met by selection of Fe^{3+} as the B site cation because of the good orbital energy match with oxide, enhancing the exchange constant J, and the large S = 5/2 spin of the d^5 cations in a mean-field approximation to the magnetic ordering temperature $T_{ord} \approx zJS(S+1)/k_B$ (where z is the number of nearest neighbor cations and k_B is Boltzmann's constant). Fe^{3+}-O^{2-}-Fe^{3+} interactions are dominantly antiferromagnetic (AFM) when driven by conventional superexchange alone, but antisymmetric exchange between two Fe^{3+} cations without an inversion center between them can create canted spontaneous magnetization via the Dzyaloshinskii-Moriya mechanism, as in the weak ferromagnet α-Fe_2O_3 (*18, 19*). Imposing the correct combination of octahedral tilts on an Fe^{3+} -based material could simultaneously generate spontaneous magnetization and polarization at RT.

The Fe^{3+} n = 2 RP phases $BaLa_2Fe_2O_7$ and $SrLa_2Fe_2O_7$ are untilted and adopt the nonpolar space group *I4/mmm* (Fig. 1). They order antiferromagnetically below 545 (*21*) and 535 K

(*22*), respectively, demonstrating that Fe-based n = 2 RP oxides offer high-temperature magnetic ordering. Chemical substitutions are required to produce the three coupled octahedral tilts of the polar $(a^-a^-c^+)/(a\text{-}a\text{-}c_+)$ tilt system. Here $a\text{-}a\text{-}$ signifies out-of-phase tilts of equal magnitude about orthogonal axes in the basal plane, and c_+ signifies an in-phase rotation of different magnitude about the stacking axis, with the brackets referring to the two $(ABO_3)_2$ blocks within the unit cell (Fig. 1). Introduction of a smaller lanthanide (*Ln*) cation induces rotation of the octahedral network to reduce the A site coordination number *e.g.*, $SrTb_2Fe_2O_7$ was reported as a uniquely distorted n = 2 RP phase (*23*) which exhibits a Néel temperature (T_N) of 542 K (*24*), but reinvestigation of this compound by density functional theory (DFT) calculations predicts a conventional single octahedral rotation in the nonpolar $(a^-b^0c^0)/(b^0a^-c^0)$ tilt scheme (Fig. 1). The synthetically accessible phase was $Sr_{1.1}Tb_{1.9}Fe_2O_7$ (fig. S1, S2 and (*25*)), and its refined crystal structure (Fig. 2A) adopts the tilt scheme predicted by DFT. The generation of a polar structure requires two further tilts to yield the $(a^-a^-c^+)/(a^-a^-c^+)$ tilt system, but this is not accessible with any Sr/*Ln* combination within the stability limits of the n = 2 RP structure (*25*).

Tilting in perovskites is driven by the need to compensate for under-bonding caused by reduction of the A site cation size, so we performed DFT calculations to evaluate the potential effect of substituting Ca^{2+} for Sr^{2+} in $SrTb_2Fe_2O_7$ to afford $CaTb_2Fe_2O_7$. The calculations show that Ca^{2+} is underbonded with less than three tilts [see bond valence sums (BVSs) in calculated structures, Table 1], so introduction of Ca^{2+} should drive polarization by inducing a third (c^+) tilt. However, the calculations also indicate that it may be necessary to compensate the loss of bonding at Fe^{3+} to stabilize the polar *A2₁am* structure (Fig. 1), which must be done without destroying the magnetism. The Tb^{3+} BVS is satisfied with one tilt but, unlike the Fe^{3+} BVS, it is not substantially affected by the key third (c^+) tilt.

We next explored the synthesis of three-tilt polar n = 2 RP phases. $CaTb_2Fe_2O_7$ itself could not be synthesized (because of phase separation to the n = 1 RP phase plus perovskite) but additional tilts were induced in the series $(Sr_{1-y}Ca_y)_{1.15}Tb_{1.85}Fe_2O_7$ for $0.55 \leq y < 0.65$ (fig. S3). Neutron powder diffraction (NPD) measurements (fig. S6 and S7), which are highly sensitive to oxygen displacements, showed that these materials exhibited the two a^- tilts shown in Fig. 1 plus a disordered c^+ tilt (*26*), validating the synthetic strategy of introducing this in-phase tilt by Ca^{2+} substitution (Fig. 2B). The disordered nature of the c^+ tilt produced nonpolar *Amam* symmetry at room temperature. The *Amam* crystal structure was unchanged on cooling to 40 K. The magnetic ordering exhibited by this series was purely antiferromagnetic and persisted to high temperatures, *e.g.*, the y = 0.60 member $(Ca_{0.60}Sr_{0.40})_{1.15}Tb_{1.85}Fe_2O_7$ has a T_N of 525 K (fig. S7 and S13).

The presence of the disordered third tilt suggests that the *Amam* structure in the $(Sr_{1-y}Ca_y)_{1.15}Tb_{1.85}Fe_2O_7$ series is near the target polar instability. Further substitution of Ca^{2+} into this series is not possible beyond y = 0.65 (fig. S3), so a different route was needed to order the c^+ tilt and access the polar structure. We coupled the further substitution of Ca^{2+} for Sr^{2+} with the replacement of Fe^{3+} (r = 0.645Å) with Ti^{4+} (r = 0.605Å) (*27*) to stabilize the structure by compensating for the under-bonding at the B site that the third tilt brings (Table 1). We synthesized two series of solid solutions between purely AFM $[1\text{-}x](Ca_ySr_{1-y})_{1.15}Tb_{1.85}Fe_2O_7$ ("CSTF" with y = 0.60 or 0.563) and nonmagnetic $[x]Ca_3Ti_2O_7$ ("CTO", which adopts the polar three-tilt structure), which formed stable n = 2 RP phases across the range $0.0 \leq x \leq 0.30$. Examination of the variation of the lattice parameters with x at RT showed a well-defined minimum and gradient change in the c/b ratio at x = 0.13 for both the y = 0.60 series (Fig. 2E) and the y = 0.563 series (fig. S22), suggesting that a compositionally-driven structural phase transition occurred. Refinement of NPD data (fig. S4) shows that at and beyond this minimum, the materials with x > 0.13 adopt the targeted polar *A2₁am* RT

structure because of the onset of an ordered c^+ tilt, described by the X^{2+} distortion mode (Fig. 2E inset and fig. S11) and accompanied by a marked increase in the intensity of the (313) nuclear reflection (Fig. 2F). The refined polar RT structure of x = 0.20, y = 0.60 with the ($a^-a^-c^+$)/($a^-a^-c^+$) tilt system is shown in Fig. 2C, alongside the polarization arising from the three tilts (Fig. 2D) which is amplified by the observed A-site cation ordering because the smaller and more highly charged Tb^{3+} cations preferentially occupy the lower coordination number A-sites in the rock salt layer (table S1 and S2). The RT NPD refinement of x = 0.17, y = 0.60, which is polar and weakly ferromagnetic up to 315 K, is shown in fig. S10. For $0.05 \leq x \leq 0.13$, the ordering of the c^+ tilt occurs on cooling from room temperature, with the structural transition temperature T_{c+} signaled by the same minimum in c/b (fig. S16 and S20).

All of the materials ($0.0 \leq x \leq 0.30$) in both the $(Ca_{0.60}Sr_{0.40})_{1.15}Tb_{1.85}Fe_2O_7$ (y = 0.60)- and $(Ca_{0.563}Sr_{0.437})_{1.15}Tb_{1.85}Fe_2O_7$ (y = 0.563)-based series order magnetically. The magnetic structure was directly affected by the chemically-induced polar c_+ tilt. Materials adopting the nonpolar *Amam* crystal structure display AFM order in magnetic space group P_Bnnm, which has point symmetry *mmm1'* (Fig. 3A and fig. S12). This magnetic symmetry forbids weak ferromagnetism (*28*) confirmed by the observation of linear M(H) isotherms for phases adopting this structure (Fig. 3E and fig. S21). The transition into the polar $A2_1am$ crystal structure driven by the c_+ tilt changed the magnetic structure, signaled by the appearance of the strong (102) magnetic Bragg reflection (Fig. 3C). The tilt drove reorientation of the spins by 180° between the two perovskite blocks in the unit cell, affording magnetic space group $A2_1'a'm$ (Fig. 3A and fig. S12). The point symmetry *2'm'm* now permitted weak ferromagnetic (WFM) canting of the Fe^{3+} moments in these polar materials (*28*), demonstrated by nonlinear, hysteretic M(H) isotherms for phases adopting this magnetic structure (Fig. 3E and fig. S21). The onset of weak ferromagnetism in the dc magnetization measurements coincided with the appearance of the $A2_1'a'm$ magnetic structure (Fig. 3B for y = 0.60, and fig. S23 and S24 for y = 0.563). The Bragg scattering signaling long-range bulk magnetic order in the polar $A2_1am$ crystal structure was accompanied simultaneously by a sharp increase in M(T) because of the spin canting (Fig. 3D). These observations both show that the observed magnetization was determined by the bulk magnetic structure of the n = 2 RP phase: the weak ferromagnetism was produced by canting of the moments in the polar structure due to the c^+ tilt. For compositions with $0.13 < x < 0.20$, y = 0.60, the two magnetic structures co-exist at room temperature, with the canted magnetic structure becoming dominant when x > 0.15 (Fig. 3B).

We plot T_N, T_{c+}, and temperature dependence of the magnetic structures determined by neutron diffraction (fig. S13 – 16) together with the magnetization onset temperatures (T_{wfm} and T_{max}) from dc M(T) scans (fig. S17 – 19) to produce the phase diagram in Fig. 4A, which demonstrates the interplay between c^+ tilt, magnetization and magnetic structure. The structural and magnetic properties of the y = 0.563 series are consistent with those of the y = 0.60 series (fig. S22 – 24). T_N decreased with x from 525 K in x = 0.0, y = 0.60, as nonmagnetic Ti^{4+} substitutes for Fe^{3+}, while T_{c+} increased because of the higher Ca^{2+} content to 693 K for x = 0.30, y = 0.60. These opposing trends produced four regions in the phase diagram, with the nature of the magnetic order controlled by the tilt: nonpolar AFM or polar WFM ground states are accessible, but there is no polar AFM state. The coexistence of weak ferromagnetism and polarization can persist to 330 K in the y = 0.60 series, with nonzero remanent magnetic moments above RT for the polar compositions between $0.13 < x < 0.20$ (Fig. 4B). The c^+ tilt thus produces both structurally-detectable electrical polarization and spontaneous magnetization at RT for the compositions $0.13 < x < 0.20$, y = 0.60.

The parent composition x = 0.0, y = 0.60 is located in the nonpolar AFM region of Fig. 4A and does not show linear magnetoelectric (ME) coupling (fig. S28), consistent with the

magnetic and crystal symmetries determined above (*28*). The symmetry of the WFM polar structure region permits linear ME coupling (ME susceptibility $\alpha = \mu_0 M/E$ (*25, 28*)) which was observed in pellets of both series in this region of the phase diagram (fig. S28 for y = 0.60 and fig. S29, S30 for y = 0.563). ME experiments were conducted at 60 and 100 K, thus avoiding artifacts caused by leakage currents (fig. S27). A linear ME coupling was exhibited by all $x \neq 0$ compositions in the polar WFM region of the phase diagram (Fig. 4C). NPD refinements and M(H) loops at the ME measurement temperatures show that these compositions all exhibited the same polar crystal structures and canted magnetic structures as found at RT (fig. S22, S23 and S25). The size of the ME coupling increased with the magnitude of the c^+ tilt despite the complex composition-dependence of the saturated Fe moment: at 60 K the competition between increased canting and dilution of the Fe sublattice produces a maximum saturated moment at $x \approx 0.13$ (fig. S26), while the maximum α was observed at x = 0.30 where the c^+ tilt amplitude is greatest (Fig. 4C). This increase in α with x shows that the enhanced tilt (T_{c+} increased with x), which induced both polarization and magnetization, overcame the reduced strength of the magnetic exchange (T_N decreased with x) and controlled the ME coupling, in accordance with the x dependence of the structural and magnetic phase boundaries seen in Fig. 4A.

A single set of cooperative atomic motions (the c^+ tilt) was imposed by designed chemical substitution into the parent n = 2 Ruddlesden-Popper $A_3B_2O_7$ structure to produce RT polarization and magnetization simultaneously. As these two often antagonistic order parameters both arise from the chemically-driven tilting of the oxygen network, ensuring that the resulting polarization is large enough to be structurally detectable, their coupling is observed in the ME response, although the magnetization arises from the Fe 3*d* electrons whereas the polarization is produced by relative displacement of all of the constituent ions. Ferroelectric switching of the polarization will require higher electric fields than we access here, enabled by ceramic engineering to minimize loss (*29*). Using a strongly magnetic B site sublattice along with the A site composition to control the tilt structure, we synthesized materials that are both polar and weakly ferromagnetic at up to 330 K over a range of compositions, revealing the potential of crystal-chemically driven symmetry control to generate multiple coupled functions.

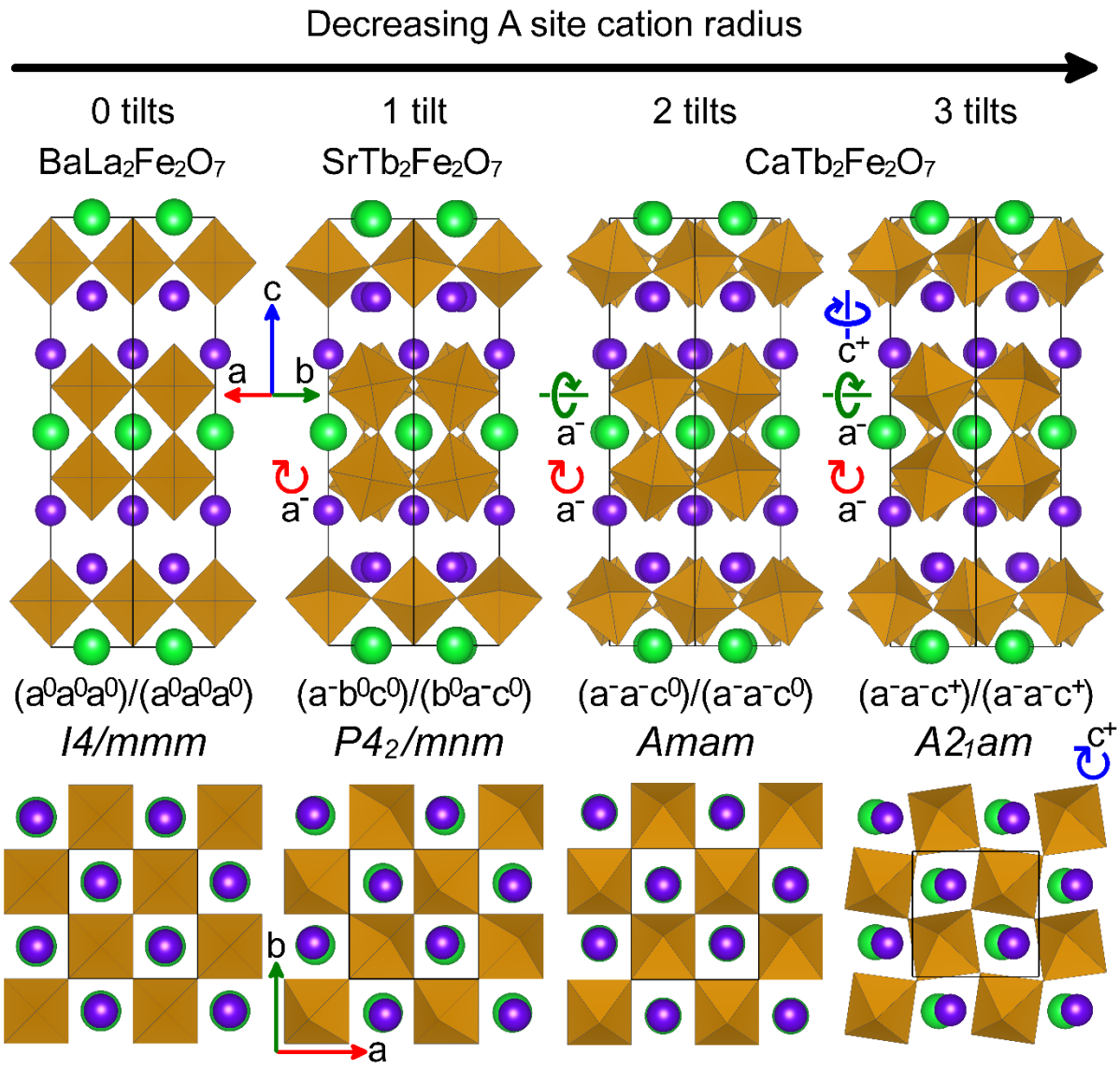
Decreasing A site cation radius
0 tilts
1 tilt
2 tilts
3 tilts
BaLa2Fe2O7
SrTb2Fe2O7
CaTb2Fe2O7
c
a
b
a-
a-
a-
a-
c+
a-
a-
(a0a0a0)/(a0a0a0)
(a-b0c0)/(b0a-c0)
(a-a-c0)/(a-a-c0)
(a-a-c+)/(a-a-c+)
I4/mmm
P42/mnm
Amam
A21am
c+
b
a

Fig. 1. *Crystal chemical engineering of octahedral tilts in the n = 2 RP structure. Lowest-energy crystal structures and space group symmetries obtained by DFT calculations are shown for the previously reported compounds $BaLa_2Fe_2O_7$ and $SrTb_2Fe_2O_7$, and the hypothetical compound $CaTb_2Fe_2O_7$ where two candidate structures are shown. Reducing the A site cation size from $BaLa_2Fe_2O_7$ to $SrTb_2Fe_2O_7$ introduces a single tilt. DFT calculations predict that reducing the A site cation size further to form $CaTb_2Fe_2O_7$ would produce a polar structure in space group $A2_1am$ with three tilts, which is found to be lower in energy than the zero, one or two tilt structures shown. Tilt axes are shown with arrows, and are labelled according to Glazer notation (20), along with the space-group symbol of the resulting structure. Alkaline earth atoms are shown in green, lanthanides in purple and FeO_6 octahedra in brown.*

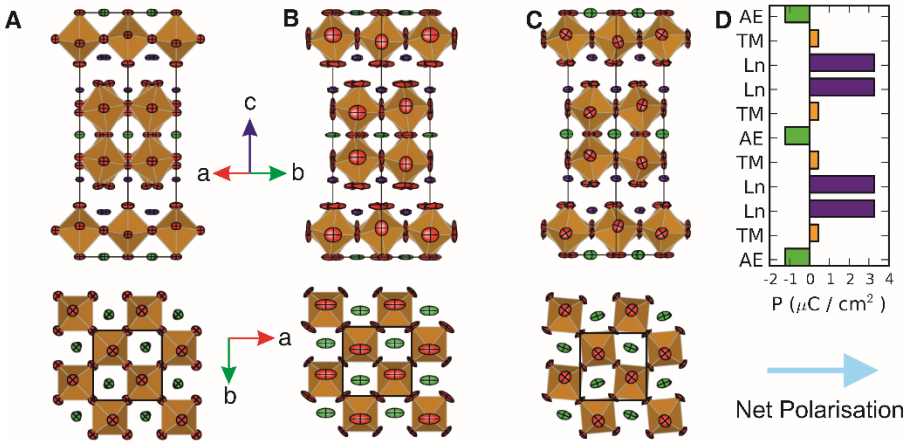

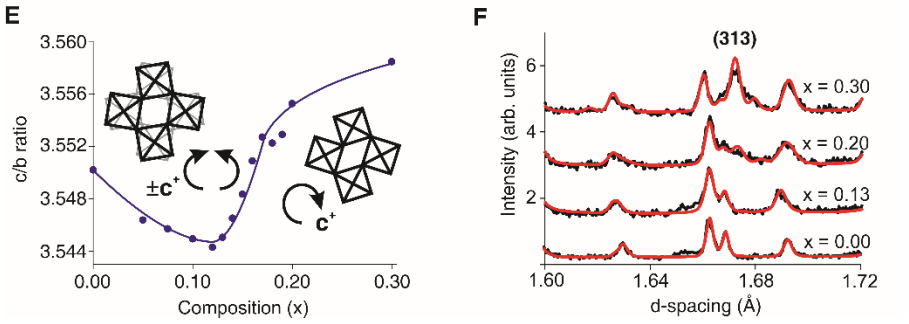

Fig. 2. *The onset of an ordered c^+ tilt as a function of composition in the system $[1-x](Ca_ySr_{1-y})_{1.15}Tb_{1.85}Fe_2O_7$-$[x]Ca_3Ti_2O_7$, y = 0.563 and 0.60 (A) Refined crystal structure of $Sr_{1.1}Tb_{1.9}Fe_2O_7$ from NPD, which exhibits a single $(a^-b^0c^0)/(b^0a^-c^0)$ tilt in space group $P4_2/mnm$, projected along [110] and [001] with atoms plotted as 99% probability ellipsoids and FeO_6 plotted as solid octahedra. (B) Refined structure of x = 0.10, y = 0.60 from NPD, a non-polar two-plus-disordered-third tilt system $(a^-a^-c^{<0>})/(a^-a^-c^{<0>})$ in space group Amam. The disordered c^+ tilt, indicated as $c^{<0>}$, can be described using either anisotropic displacement parameters highly elongated along the in-plane directions orthogonal to the tilt axis (used here for simple comparison with the other materials shown) or with the split site model shown in fig. S5A. (C) Refined structure of x = 0.20, y = 0.60 which adopts a polar three-tilt system $(a^-a^-c^+)/(a^-a^-c^+)$ in space group $A2_1am$, (D) Layer-by layer polarisation of $A2_1am$ x = 0.20, y = 0.60, calculated from the refined structure in (C), showing a net polarisation along the a-axis (AE = alkaline earth oxide, TM = transition metal oxide, Ln = lanthanide oxide). (E) c/b ratio plotted as a function of composition for series y = 0.60 in the range $0.0 \leq x \leq 0.30$ at room temperature, with schematic illustration of the ordered c^+ tilt onset shown inset, (F) NPD data showing the emergence of the (313) nuclear Bragg reflection as polarity*

increases in the series y = 0.563 - the intensity of this reflection cannot be fitted in Amam (fig. S8).

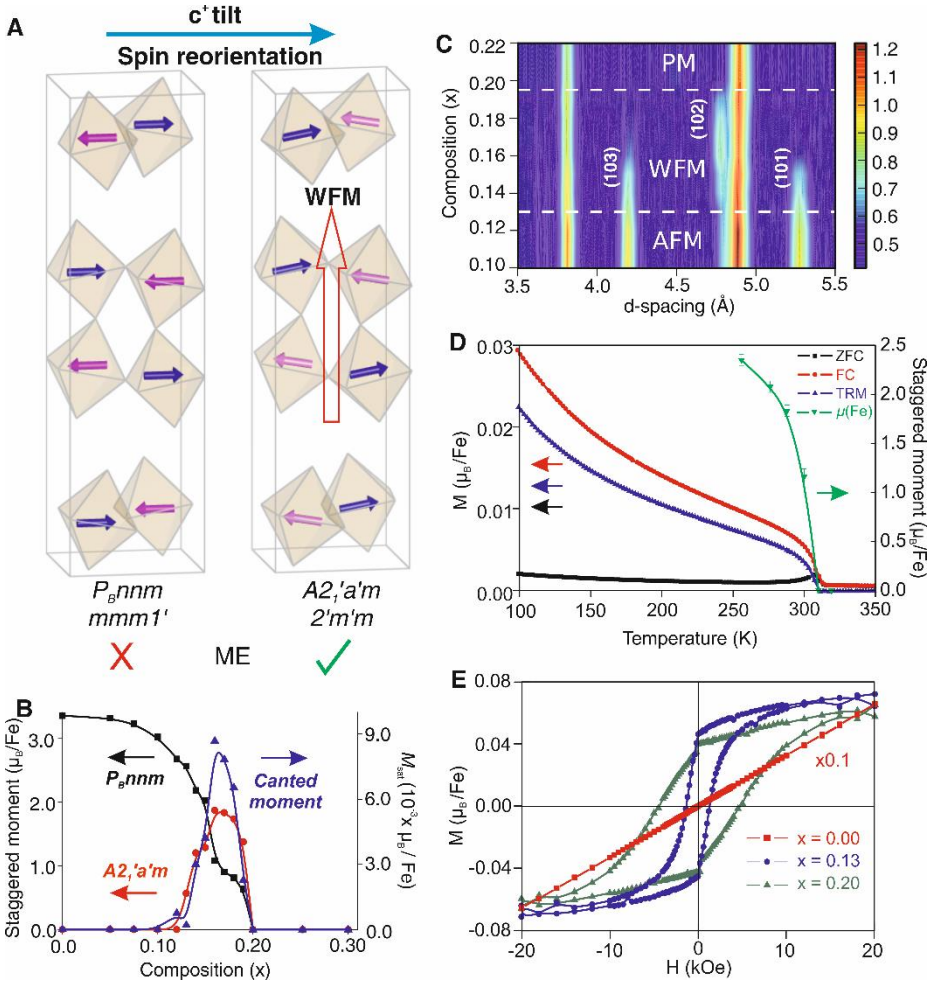

Fig. 3. *Simultaneous magnetic spin-reorientation transition and onset of weak ferromagnetism at the transition to a polar crystal structure as a function of composition. (A) The $P_B$nnm and $A2_1$'a'm magnetic structures, with the magnetic Fe^{3+} sublattice illustrated as blue/pink arrows. The transition from the $P_B$nnm to the $A2_1$'a'm magnetic structure occurs with retention of the G-type ordering within the perovskite blocks, but changes the ordering between the blocks (see also fig. S12), to allow spin canting and magnetoelectric (ME) coupling in the polar materials. (B) Refined antiferromagnetically ordered (staggered) Fe moment (25) in each magnetic structure from NPD, and canted moment from M(H) loops at 300 K, plotted versus composition at room temperature for series $0.0 \leq x \leq 0.30$, $y = 0.60$, showing the onset of the spin-canted $A2_1$'a'm structure at $x = 0.13$. (C) Contour plot constructed from 10 room temperature NPD patterns in the compositional range $0.10 \leq x \leq 0.20$, $y = 0.60$ (GEM diffractometer, $2\theta = 35°$ detector bank) showing the magnetic transitions from the AFM ($P_B$nnm) structure to the WFM ($A2_1$'a'm) structure to paramagnetic (PM) with increasing x. The magnetic peaks are labelled with their hkl indices to distinguish them from the nuclear Bragg peaks persisting throughout the composition range. (D) M(T) data and refined staggered Fe moment from NPD for the polar phase $x = 0.18$, $y = 0.60$, showing the onset of WFM at $T_N = 310$ K, as indicated by a sharp increase in thermoremanent magnetization (TRM), splitting of the field-cooled (FC) and zero-field cooled (ZFC) data and the appearance of magnetic Bragg peaks from the $A2_1$'a'm magnetic structure in the NPD patterns. (E) M(H) loops at the magnetoelectric measurement temperature (60 K) for samples of $x = 0.13$, 0.20 ($y = 0.563$), with linear contribution*

subtracted (fig. S25), and non-subtracted data with an applied scale factor of 0.12 plotted for x = 0.0, y = 0.563.

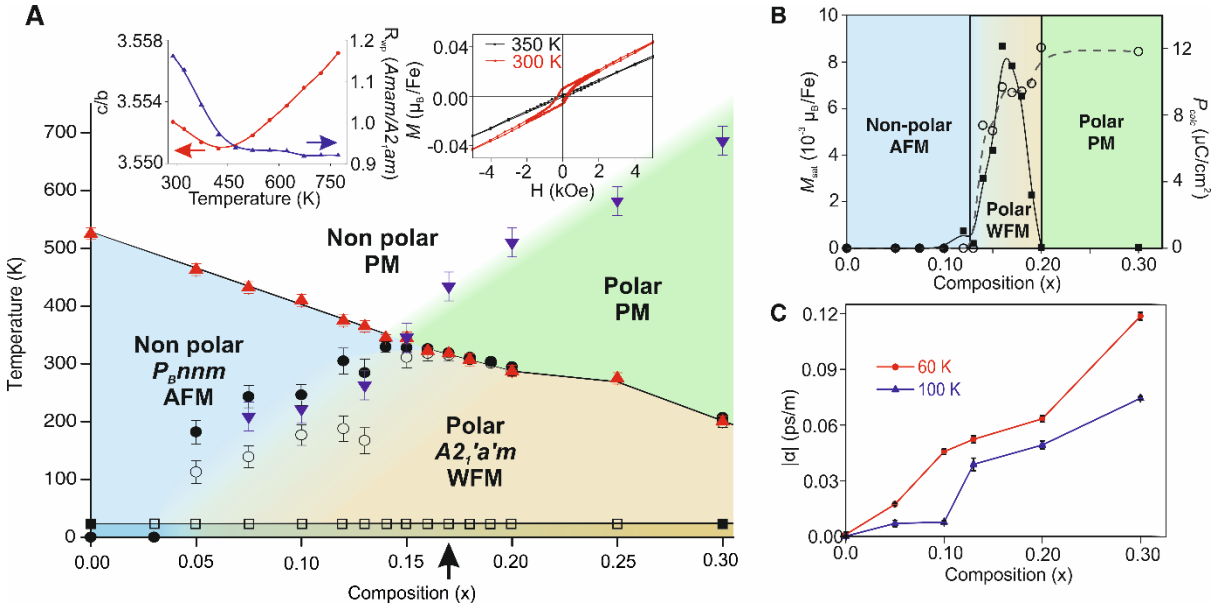

Fig. 4. *Phase diagram of the series 0.0 ≤ x ≤ 0.30, y = 0.60 and the occurrence of magnetoelectric (ME) coupling in the polar/weak ferromagnetic region (A) Structural-magnetic phase diagram showing dependence of crystal structure (polarity), magnetic structure and magnetisation on composition and temperature in the series [1-x] $(Ca_ySr_{1-y})_{1.15}Tb_{1.85}Fe_2O_7$-[x]$Ca_3Ti_2O_7$ with y = 0.60. Red triangles = T_N from NPD (fig. S13 – S15); blue inverted triangles = T_{c+} from c/b ratio plots (fig. S14); black circles = T_{wfm} (onset WFM) from divergence of field-cooled and zero-field cooled M(T) plots (fig. S16 – S18); open circles = T_{max} from maxima in |∂M(T)/∂T| plots (fig. S17 – S19); black squares = Tb^{3+} magnetic ordering from NPD; open squares = Tb^{3+} magnetic ordering from M(T) plots. Four distinct regions are marked by colour blocks which correspond to paramagnetic (PM)/non-polar (white); PM/polar (green); $A2_1'a'm$/WFM/polar (orange); and P_Bnnm/AFM/non-polar (blue). Insets show the polar-nonpolar transition at 450 K by the temperature dependence of the lattice parameters (c/b ratio) and the ratio of R_{wp} values for Amam and $A2_1am$ models, and the presence of WFM at 300 K by M(H) loop, for x = 0.17 (marked with a black arrow on the x-axis). (B) Cross-section of the phase diagram (A) at 300 K: saturated magnetic moment per Fe from M(H) loops (fig. S21, black squares, with solid line as a guide to the eye) plotted with calculated polarisation of the refined crystal structure from NPD (open circles, with dashed line as a guide to the eye) showing the simultaneous emergence of magnetisation and polarisation as x increases, with regions colored to correspond with those mapped in (A). (C) Linear ME susceptibility α vs composition at 60 and 100 K for the series 0.0 ≤ x ≤ 0.30, y = 0.563, showing that the ME coupling increases with polarisation.*

Table 1. *The energies of the relaxed structures of $CaTb_2Fe_2O_7$ with polar and non-polar tilt schemes. Energies are calculated by DFT, and quoted relative to the calculated energy in the polar $A2_1am$ structure.*

Tilt Scheme	Relative Energy (eV / Formula Unit)	BVS (Fe)	BVS (Ca)	BVS (Tb)
$(a^-a^-c^+)/(a^-a^-c^+)$	0	2.80	1.80	3.02
$(a^-a^-c^0)/(a^-a^-c^0)$	0.17	2.99	1.58	2.94
$(a^-b^0c^0)/(b^0a^-c^0)$	0.10	2.99	1.47	2.99
$(a^0a^0a^0)/(a^0a^0a^0)$	0.95	3.34	1.16	2.71

References and Notes:

1. L.-D. Zhao *et al.*, Ultralow thermal conductivity and high thermoelectric figure of merit in SnSe crystals. *Nature* **508**, 373-377 (2014).
2. H. Sakai *et al.*, Displacement-Type Ferroelectricity with Off-Center Magnetic Ions in Perovskite $Sr_{1-x}Ba_xMnO_3$. *Phys. Rev. Lett.* **107**, 137601 (2011).
3. N. A. Hill, Why are there so few magnetic ferroelectrics? *J. Phys. Chem. B* **104**, 6694-6709 (2000).
4. M. Bibes, A. Barthelemy, Multiferroics: Towards a magnetoelectric memory. *Nature Mater.* **7**, 425-426 (2008).
5. C. A. F. Vaz, Electric field control of magnetism in multiferroic heterostructures. *J. Phys. Cond. Matter* **24**, 333201 (2012).
6. D. M. Evans *et al.*, Magnetic switching of ferroelectric domains at room temperature in multiferroic PZTFT. *Nature Commun.* **4**, 1534 (2013).
7. J. van Suchtelen, Product properties: a new application of composite materials. *Philips Res. Rep.* **27**, 28-37 (1972).
8. N. J. Perks, R. D. Johnson, C. Martin, L. C. Chapon, P. G. Radaelli, Magneto-orbital helices as a route to coupling magnetism and ferroelectricity in multiferroic $CaMn_7O_{12}$. *Nature Commun.* **3**, 1277 (2012).
9. M. Ghita, M. Fornari, D. J. Singh, S. V. Halilov, Interplay between A-site and B-site driven instabilities in perovskites. *Phys. Rev. B* **72**, 054114 (2005).
10. N. A. Benedek, C. J. Fennie, Hybrid improper ferroelectricity: A mechanism for controllable polarization-magnetization coupling. *Phys. Rev. Lett.* **106**, 107204 (2011).
11. J. M. Rondinelli, C. J. Fennie, Octahedral rotation-induced ferroelectricity in cation ordered perovskites. *Adv. Mater.* **24**, 1961-1968 (2012).
12. K. S. Aleksandrov, J. Bartolome, Octahedral tilt phases in perovskite-like crystals with slabs containing an even number of octahedral layers. *J. Phys. Cond. Matter* **6**, 8219-8235 (1994).
13. J. Alaria *et al.*, Engineered spatial inversion symmetry breaking in an oxide heterostructure built from isosymmetric room-temperature magnetically ordered components. *Chem. Sci.* **5**, 1599-1610 (2014).
14. M. M. Elcombe *et al.*, Structure determinations for $Ca_3Ti_2O_7$, $Ca_4Ti_3O_{10}$, $Ca_{3.6}Sr_{0.4}Ti_3O_{10}$ and a refinement of $Sr_3Ti_2O_7$. *Acta Crystallogr.* **B47**, 305-314 (1991).
15. Y. S. Oh, X. Luo, F.-T. Huang, Y. Wang, S.-W. Cheong, Experimental demonstration of hybrid improper ferroelectricity and presence of abundant charged walls in $(Ca,Sr)_3Ti_2O_7$ crystals. *(available at http://arxiv.org/abs/1411.6315)*.
16. Y. Yoshida *et al.*, Crystal and magnetic structure of $Ca_3Ru_2O_7$. *Phys. Rev. B* **72**, 054412 (2005).
17. M. V. Lobanov *et al.*, Crystal and magnetic structure of the $Ca_3Mn_2O_7$ Ruddlesden-Popper phase: neutron and synchrotron x-ray diffraction study. *J. Phys. Cond. Matter* **16**, 5339-5348 (2004).
18. I. E. Dzialoshinskii, Thermodynamic theory of weak ferromagnetism in antiferromagnetic substances. *Sov. Phys. JETP* **5**, 1259-1272 (1957).
19. T. Moriya, Anisotropic superexchange interaction and weak ferromagnetism. *Phys. Rev.* **120**, 91-98 (1960).
20. A. M. Glazer, The classification of tilted octahedra in perovskites. *Acta Crystallogr.* **B 28**, 3384-3392 (1972).
21. D. Samaras, A. Collomb, Rotation of magnetic-moments in $BaLa_2Fe_2O_7$. *Solid State Commun.* **16**, 1279-1284 (1975).
22. N. N. M. Gurusinghe *et al.*, Synthesis and characterisation of the n = 2 Ruddlesden–Popper phases $Ln_2Sr(Ba)Fe_2O_7$ (Ln = La, Nd, Eu). *Mater. Res. Bull.* **48**, 3537-3544 (2013).
23. D. Samaras, A. Collomb, J. C. Joubert, Determination of structures of 2 new mixed ferrites having formula $BaLa_2Fe_2O_7$ and $SrTb_2Fe_2O_7$. *J. Solid State Chem.* **7**, 337-348 (1973).
24. D. Hanžel, $SrTb_2Fe_2O_7$ studied by Mössbauer spectra of ^{57}Fe. *J. Magn. Magn. Mater.* **5**, 243-246 (1977).
25. Materials and methods are available as supplementary material on Science Online.
26. Crystallographic information files may be obtained from Fachinformationszentrum Karlsruhe, 76344 Eggenstein-Leopoldshafen, Germany (e-mail: crysdata@fiz-karlsruhe.de, http://www.fiz-karlsruhe.de/request_for_deposited_data.html) on quoting the appropriate CSD number tabulated in Table S2.
27. R. D. Shannon, C. T. Prewitt, Effective Ionic Radii in Oxides and Fluorides. *Acta Crystallogr.* **B 25**, 925-946 (1969).
28. H. Schmid, Some symmetry aspects of ferroics and single phase multiferroics. *J. Phys. Cond. Matter* **20**, 434201 (2008).

29. I. M. Reaney *et al.*, Defect chemistry of Ti-doped antiferroelectric $Bi_{0.85}Nd_{0.15}FeO_3$. *Appl. Phys. Lett.* **100**, 182902 (2012).
30. G. Kresse, J. Furthmüller, Efficient iterative schemes for ab initio total-energy calculations using a plane-wave basis set. *Phys. Rev. B* **54**, 11169-11186 (1996).
31. G. Kresse, D. Joubert, From ultrasoft pseudopotentials to the projector augmented-wave method. *Phys. Rev. B* **59**, 1758-1775 (1999).
32. J. P. Perdew, K. Burke, M. Ernzerhof, Generalized gradient approximation made simple. *Phys. Rev. Lett.* **77**, 3865-3868 (1996).
33. S. L. Dudarev, G. A. Botton, S. Y. Savrasov, C. J. Humphreys, A. P. Sutton, Electron-energy-loss spectra and the structural stability of nickel oxide: An LSDA+U study. *Phys. Rev. B* **57**, 1505-1509 (1998).
34. N. E. Brese, M. O'Keeffe, Bond-valence parameters for solids. *Acta Crystallogr.* **B47**, 192-197 (1991).
35. S. P. Thompson *et al.*, Beamline I11 at Diamond: A new instrument for high resolution powder diffraction. *Rev. Sci. Instrum.* **80**, 075107 (2009).
36. M. E. Fisher, Relation between the specific heat and susceptibility of an antiferromagnet. *Philos. Mag.* **7**, 1731-1743 (1962).
37. J. M. D. Coey, J. T. Mlack, M. Venkatesan, P. Stamenov, Magnetization process in dilute magnetic oxides. *IEEE Trans. Magn.* **46**, 2501-2503 (2010).
38. P. Borisov, A. Hochstrat, V. V. Shvartsman, W. Kleemann, Superconducting quantum interference device setup for magnetoelectric measurements. *Rev. Sci. Instrum.* **78**, 106105 (2007).
39. M. Fiebig, Revival of the magnetoelectric effect. *J. Phys. D: Appl. Phys.* **38**, R123 (2005).
40. D. Samaras, A. Collomb, J. C. Joubert, E. F. Bertaut, Magnetic study of $SrTb_2Fe_2O_7$ - determination of magnetic-structures by neutron-diffraction. *J. Solid State Chem.* **12**, 127-134 (1975).
41. S. Kerman *et al.*, The superstructure determination of displacive distortions via symmetry-mode analysis. *Acta Crystallogr.* **A68**, 222-234 (2012).
42. M. A. Green, D. A. Neumann, Synthesis, structure, and electronic properties of $LaCa_2Mn_2O_7$. *Chem. Mater.* **12**, 90-97 (2000).
43. I. A. Zvereva, S. R. Seitablaeva, Y. E. Smirnov, Cation distribution and interatomic interactions in oxides with heterovalent isomorphism: VI. solid Solutions $Nd_2Sr_{1-x}Ca_xAl_2O_7$. *Russ. J. Gen. Chem.* **73**, 31-36 (2003).
44. I. A. Zvereva, A. G. Cherepova, Y. E. Smirnov, Cation distribution and interatomic interactions in oxides with heterovalent isomorphism: XII. $Gd_2Sr_{1-x}Ca_xAl_2O_7$ solid solutions. *Russ. J. Gen. Chem.* **77**, 517-523 (2007).

Acknowledgments: This work is funded by the European Research Council (ERC Grant agreement 227987 RLUCIM). Synchrotron X-ray diffraction work was carried out with the support of Diamond Light Source (UK). Time-of-flight neutron diffraction work was carried out with the support of ISIS Spallation Source (UK). We thank Dr. C. Tang, Dr. S. Thompson, Dr. J. Parker and Dr. P. Adamson for assistance on beamline I11 (DLS), Dr W. Kockelmann and Prof. D. Keen for assistance on GEM (ISIS), Dr. A. Daoud-Aladine and Dr. K. Knight for assistance on HRPD (ISIS), and Dr. R. Smith for assistance on POLARIS (ISIS). Computational resources were provided and funded by the N8 consortium and EPSRC (EP/K000225/1) and the UK's national high-performance computing service HECToR through the UK's HPC Materials Chemistry Consortium funded by EPSRC (EP/L000202).

Supplementary Materials
www.sciencemag.org
Materials and Methods
Supplementary text
Figs. S1 - S30
Tables S1 – S4
References (30-44)